Assessing robustness of hyperelastic models for describing nonlinearity of the mechanical response for pristine and swollen carbon black filled elastomers

H Boulman, A Mdarhri, Y Nezili, F El Haouzi, I El Aboudi, C Brosseau

Received: 29 August 2023 | Revised: 30 November 2023 | Accepted: 21 December 2023

DOI: 10.1002/app.55168

RESEARCH ARTICLE

Journal of Applied Polymer Science WILEY

Assessing robustness of hyperelastic models for describing nonlinearity of the mechanical response for pristine and swollen carbon black filled elastomers

H. Boulman[1] | **A. Mdarhri**[1] | **Y. Nezili**[1] | **F. El Haouzi**[1] | **I. El Aboudi**[1] | **C. Brosseau**[2]

[1]FSTG, Lab-RDDS, Univ. Cadi Ayyad, Marrakesh, Morocco

[2]CNRS, Lab-STICC, Univ. Brest, Brest Cedex 3, France

Correspondence
C. Brosseau, CNRS, Lab-STICC, Univ. Brest, CS 93837, 6 Avenue Le Gorgeu, 29238 Brest Cedex 3, France.
Email: brosseau@univ-brest.fr

Abstract

We consider the hyperelastic response of semi-crystalline ethylene–co-butyl acrylate (EBA) samples filled with carbon black (CB) particles. Such material is structurally complex with its microstructure being characterized by many structural parameters including crosslink density, filler/matrix interfaces, crystallinity, filler network, and chain entanglement which have different degrees of influence on the effective mechanical properties. We evaluate the ability of a number of analytical models to correctly reproduce the non-linear elastic mechanical response of these samples. We do this by considering either dry samples, or samples which are swollen by a non-polar solvent (toluene) at equilibrium, and subjected to uniaxial tension at room temperature. As test cases, we focus on six physical models for the purpose of analyzing the stress–strain curves of samples with different cross-linking densities. Among these frameworks, we show that the Mooney–Rivlin (MR), Ogden, and eight-chain models accurately describe the stress–strain curves of both dry and swollen CB-EBA samples. These findings highlight the possibility of attaining a diverse set of mechanical properties of filled polymer samples by tailoring their structural parameters.

KEYWORDS

carbon black, composite, crosslink, elastomer, hyper-elasticity, modeling

1 | INTRODUCTION

Elastomer based-materials belong to an important class of materials for their applications in seals, joints, pipes, and tires. Over the last few decades, significant efforts have been dedicated to exploring various physical and mechanical properties including reversible extensibility, fatigue resistance, and damping. Two kinds of elastomers can be distinguished.[1] On the one hand, 3D vulcanized elastomers are formed by crosslinking organic chain polymers. On the other hand, linear or branched thermoplastic elastomer are based on rigid and flexible constitutive blocks along the main chain polymer. The effective cross-linking density (ECD) affects significantly the macroscopic mechanical performances of elastomers and depends on the type and nature of the cross-links, for example, sulfur, peroxide or metal oxides.[2] Organic peroxides are often used for the vulcanization of saturated

elastomers such as ethylene propylene. Furthermore, the good stability of carbon–carbon cross-links enhances the heat resistance of the peroxide cross-linked elastomers when suitable antioxidants are included.[3] Among their many phenomenological aspects, it is expected that a critical crosslinking content has to be determined above which degradation of their mechanical properties can occur.[2]

Among those materials elastomers filled by nanoparticles, for example, carbon black (CB), graphene, carbon nanotubes are one of the most promising nanostructured materials for a number of targeted applications, due to a number of outstanding material properties that include viscosity reduction and mechanical enhancement of the matrix.[4,5] However, an optimum content of spherical nano-fillers should be found in order to ensure a good dispersion throughout the elastomer matrix without undesirable large particle agglomerates. Agglomerates are highly susceptible to produce defects where stress concentrations occur and to undergo irrecoverable mechanical deformation that severely limits their properties under static and dynamic loading.[5] In addition, for modeling viewpoint, incorporating particle fillers acts as an additional physical crosslinking process which supplements vulcanization. When the chain length exceeds some critical length, entanglements can serve also as transient crosslinks.[6]

Hyperelastic filled elastomers opened up a completely new avenue for creating nanomaterials with structural parameters that are expected to find novel applications in fields such artificial muscles.[2] Typically, hyperelasticity characterizes the ability to a given material to deform up to 1000% under small mechanical load and to return to its initial state once the load is released. Entropy decrease during deformation at temperature above the glass transition temperature along with distortion and conformation change of mobile polymer chains to form its most probable conformation provides a general understanding of this phenomenon. In fact, many frameworks have been suggested for studying the large deformations in elastomeric materials[2,7–10] dating back the pioneering study of Mooney and Rivlin to Gregory's model suggested recently.[8,11] All of these models are derived from the stored energy density function (SED) which represents the amount of recoverable elastic energy W stored in a unit volume of the material under a specific state of strain. SED relates the strain energy to the actual state of deformation and not to its history. SED should be non-negative, set to zero for the undeformed state and is invariant under coordinate transformations.[12,13]

In most of the documented studies, attempts have been focused to reproduce the classical experimental data of Treloar on unfilled vulcanized rubber to validate such hyperelastic models since it has been considered for a long time as a prototype or worst-case scenario of highly nonlinear elastic behavior.[14] For example, Paul and coworkers[14] conclude that Treloar's elastomer data provide interesting hints concerning the choice or the design of a mechanistic model. Another interesting remark is that much of these hyperelastic models were applied to unfilled elastomers, with little attention given to their filled counterparts such as CB-filled elastomers.[15–22] We should also say that, to the best of our knowledge, no study has been devoted to evaluate the robustness of hyperelastic models to describe the mechanical response of filled elastomers under free-conditions swelling.

To develop a comprehensive understanding of the large observed deformation of CB-filled EBA samples under uniaxial stretching, here we investigate how the elasticity network change caused by swelling process can influence the accuracy of the considered model. We seek to unravel the role of swelling to determine which structural parameters (crosslinks, entanglements) have the most or least mechanical consequence in modulating the mechanical ability of the material sample. An understanding of their role can reveal a design principle that can shed lights on what to engineer to attain a desired nonlinear stress–strain behavior.

In the next section, we will set the stage by reviewing analytical procedures for modeling the stress–strain curves of material samples (assumed to be isotropic, homogenous, free of hysteresis, strain rate independent, and nearly or purely incompressible) under uniaxial stretching.[9] Next, in Section 3 we briefly describe materials and methods. In Section 4, we discuss the consequences of the models reviewed in Section 1 on our experimental data. In particular, we provide some suggestions on how to select an appropriate hyperelastic constitutive model of filled polymers and its physical implications. Section 5 contains our concluding remarks.

2 | THEORETICAL BACKGROUND

2.1 | Phenomenological models

Overall, phenomenological models can be discussed[23] depending on whether SED is formulated in terms of principal stretch $\lambda_{i=1,3}$ which represents the deformed to undeformed length ratio, or strain invariant $I_{i=1,3}$ which denotes the strain invariant of the Cauchy-Green tensor of the form.

$$I_1 = tr(C), I_2 = \frac{1}{2}\left[(tr(C))^2 - tr\left(C^2\right)\right],\ I_3 = det(C), \quad (1)$$

where, C_{ij} are material constants. The SED $= W(I_1, I_2, I_3)$ is continuously differentiable with respect to all I_i. Here,

we are interested in MR, Ogden's and Shariff's models.[12,24,25] The first model is based on the strain invariants to express the SED while the last two models consider the principal stretches.

2.1.1 | Mooney–Rivlin's model

This model is an extension of the Neo-Hookean model by including a linear dependence on I_2 in SED.[23] It has been widely used to describe large elastic deformations of rubbery materials.[26,27] If we impose volume conservation during deformation, SED will depend only on I_1 and I_2 and takes the form

$$W=\sum_{i,j=0}^{N} C_{ij}(I_1-3)^i(I_2-3)^j. \tag{2}$$

Thus, the SED of the MR5 model and the true constraint σ_v are

$$\begin{aligned} W_{MR_5} = {} & C_{10}(I_1-3)+C_{01}(I_2-3)+C_{11}(I_1-3)(I_2-3) \\ & + C_{20}(I_1-3)^2+C_{02}(I_2-3)^2, \end{aligned} \tag{3}$$

$$\sigma_v = 2\left(\lambda^2-\frac{1}{\lambda}\right)\left(\frac{\partial W}{\partial I_1}+\frac{1}{\lambda}\frac{\partial W}{\partial I_2}\right). \tag{4}$$

The Cauchy stress uniaxial loading is

$$\begin{aligned} \sigma_{uniax} = {} & 2C_{10}\left(\lambda^2-\frac{1}{\lambda}\right)+2C_{01}\left(\lambda-\frac{1}{\lambda^2}\right) \\ & + 6C_{11}\left(\lambda^2-\frac{1}{\lambda}\right)\left(\lambda-\frac{1}{\lambda}+\frac{1}{\lambda^2}-1\right) \\ & + 4C_{20}\left(\lambda^2-\frac{1}{\lambda}\right)\left(\lambda^2+\frac{2}{\lambda}-3\right) \\ & + 4C_{02}\left(\lambda-\frac{1}{\lambda^2}\right)\left(2\lambda+\frac{1}{\lambda^2}-3\right). \end{aligned} \tag{5}$$

2.1.2 | Ogden's model

This model is considered as a versatile and constitutive models for simulating the mechanical behavior of a wide variety of materials including biological matter.[9,14] Now, the SED function is formulated as a finite sum of the scaled powers of the principal stretches λ_i of the right or left Cauchy-Green tensor

$$W=\sum_{k=1}^{K}\frac{\mu_k}{\alpha_k}\left[\lambda_1^{\alpha_k}+\lambda_2^{\alpha_k}+\lambda_3^{\alpha_k}-3\right], \tag{6}$$

where, μ_n and α_n are constants and can have any value satisfying the stability condition, that is, $\mu_n\alpha_n>0$ for each n.[28] When an incompressible elastomer is uniaxially stretched, the stress is

$$\sigma_{uniax}=\sum_{k=1}^{K}\frac{2\mu_k}{\alpha_k}\left[\lambda^{\alpha_k}-\lambda^{-\frac{1}{2}\alpha_k}\right]. \tag{7}$$

2.1.3 | Shariff's model

For this model,[9] the SED is parameterized as

$$W=E\sum_{i=0}^{n}\alpha_i\varphi_i(\lambda_i), \tag{8}$$

where, E is Young's modulus, α_i being material parameters ($i=0, 1, 2, 3, ..., n$) with $\alpha_0=1$, and φ_i denote smooth functions.[25]

$$\varphi(0)=\frac{2\ln(\lambda)}{3}, \tag{9}$$

$$\varphi(1)=\exp(1-\lambda)+\lambda-2, \tag{10}$$

$$\varphi(2)=\exp(\lambda-1)-\lambda, \tag{11}$$

$$\varphi(3)=\frac{(\lambda-1)^3}{\lambda^{3.6}}. \tag{12}$$

Differentiating Equation (9) yields the true stress, and reads in the case of uniaxial tension

$$\begin{aligned} \sigma_{uniax} = {} & \frac{E}{\lambda}\left[\ln(\lambda)+\alpha_1\left[e^{1-\lambda}-e^{1-\lambda^{-\frac{1}{2}}}+\lambda-\lambda^{-\frac{1}{2}}\right]\right. \\ & + \alpha_2\left[e^{\lambda-1}-e^{\lambda^{-\frac{1}{2}}-1}-\lambda+\lambda^{-\frac{1}{2}}\right] \\ & + \alpha_3\left[\frac{(\lambda-1)^3}{\lambda^{3.6}}-\frac{\left[\lambda^{-\frac{1}{2}}-1\right]^3}{\lambda^{-1.8}}\right] \\ & \left. + \alpha_4\left[[\lambda-1]^3-\left[\lambda^{-\frac{1}{2}}-1\right]^3\right]\right]. \end{aligned} \tag{13}$$

2.2 | Micromechanical models

So far, we have discussed phenomenological models of stress–strain curves. Additionally, we can look to micromechanical approaches which connect the macroscopic behavior of a given hyperelastic material to its physical/chemical structure by using statistical physics. This generically introduces specific representations of the lattice structure, for example, 3-chain, 8-chain, and extended tube models. Now, we examine the corresponding SED functions.

2.2.1 | 3-Chain model

In the three-chain model, the true polymer network is represented by 3 chains which are oriented in the principal directions, knowing that each of them is aligned with one of the eigenvectors of the isochoric right Cauchy-Green tensor located along the axes of an initially cubic cell.[9] Under deformation, the string deforms affinely with the cell and the stretch on each string corresponds to a principal stretch value.[27] Using a non-Gaussian distribution function,[9] the resulting SED function is

$$W = \frac{\mu N}{3}\sum_{k=1}^{3}\left[\sqrt{N^{-1}}\lambda_k \beta_k + \ln\left(\frac{\beta_k}{\sinh\beta_k}\right)\right], \tag{14}$$

where the main parameters are the shear modulus μ, the number of Kuhn segments N, the inverse Langevin function β, and the isochoric principal stretch λ_k, so the stress-stretch under uniaxial deformation is

$$\sigma_{uniax} = \frac{\mu}{3}\left[\lambda^2\left[\frac{3N-\lambda^2}{N-\lambda^2}\right] - \lambda^{-1}\left[\frac{3N-\lambda^{-1}}{N-\lambda^{-1}}\right]\right]. \tag{15}$$

2.2.2 | 8-Chain model

We now consider the eight-chain model which uses a representative volume element square covered by the principal directions of the right isochoric Cauchy-Green tensor containing eight chains, each being oriented according to one of the semi-diagonals of the cuboid.[14] Each chain contributes proportionally to the deformation which makes it possible to relate the elongation of each chain to the first deformation invariant. Under uniaxial deformation, the main resulting distortion ranges are denoted λ^1, λ^2, and λ^3.[9] The SED function is given by

$$W = \mu N\left[\sqrt{N^{-1}}\Lambda\beta + \ln\left(\frac{\beta}{\sinh\beta}\right)\right]. \tag{16}$$

The Cauchy stress expression is then determined as

$$\sigma_{uniax} = \frac{\mu}{3}\left[\frac{9N-\lambda^2-2\lambda^{-1}}{3N-\lambda^2-2\lambda^{-1}}\right]\left[\lambda-\lambda^{-2}\right]. \tag{17}$$

2.2.3 | Extended tube model

The extended tube model takes into account the lattice constraints of the surrounding molecular chains and the limited extensibility of the chain.[23] Accordingly, the microstructure of a hyperelastic material comprises highly entangled polymer chains.[9] These chains are assumed to be strained into a tube formed by the surrounding chain.[9] Thus, when strain is applied, the chains in the tube are assumed to deform proportionally to the macroscopic lattice. The corresponding SED function consists of two parts, that is,

$$W = \frac{\mu_c}{2}\left[\frac{\left[1-\delta^2\right]\left[I_1-3\right]}{1-\delta^2\left[I_1-3\right]} + \ln\left(1-\delta^2\left[I_1-3\right]\right)\right] + \sum_{i=3}^{3}\frac{2\mu_e}{\beta^2}\left[\lambda_i^{-\beta}-1\right] + k(J-1)^2. \tag{18}$$

The first part of the right-hand side considers the energy of the network reticulation, while the second part represents the energy of the stresses of the confinement tube. For uniaxial loading, the true stress can be deduced from the SED function and reads

$$\sigma_{uniax} = \mu_c\left[\lambda-\lambda^{-2}\right]\left[\frac{1-\delta^2}{\left[1-\delta^2\left[I_1-3\right]\right]^2} - \frac{\delta^2}{\left[1-\delta^2\left[I_1-3\right]\right]}\right] + \frac{2\mu_e}{\beta}\left[\lambda^{\frac{\beta}{2}-1}-\lambda^{-\beta-1}\right], \tag{19}$$

where, μ_c, μ_e, δ, and β are material parameters. For the purpose of our discussion, Table 1 summarizes the important parameters of the set of models used here.

Appendix A details the different steps which allow determining the Cauchy stress (true stress) from the SED of the considered hyperelastic models for uniaxial tension.

TABLE 1 A summary of the parameters of the phenomenological and micromechanical models used in our analysis.

		Model	Year	Stability condition	Parameters	Physical meaning
Phenomenological models	Invariants based $W(I_i)$	MR	1940	-	$[C_{10}, C_{01}, C_{10}, C_{20}, C_{02}]$	C_{10}(chemical bonds) : $n = \frac{\lvert C_{10}\rvert}{RT}$ C_{01}(physical bonds) : deviation of linearity
	Stretch based $W(\lambda_i)$	Ogden	1972	$[\mu_k\, \alpha_k > 0]$	$[\mu_1, \mu_2, \mu_3, \alpha_1, \alpha_2, \alpha_3]$	$\sum_k [\mu_k\, \alpha_k = 2\mu]$ (μ classical shear modulus)
		Shariff	2000	$\alpha_1 \in [0,1.9] \in [0,0.15]$ $\alpha_2, \alpha_3 \in [0,2.3\,\alpha_2]$ $\alpha_{k+2} \geq 0$ $\alpha_{i+3} \in \left[0, \frac{k+1}{k+2}\,\alpha_{k+2}\right]$ $(k = 2j, j = 1, 2, \ldots)$	$[E, \alpha_1, \alpha_2, \alpha_3, \alpha_4]$	-
Micromechanical models		Three-chain	1943		$[\mu, N]$	μ: shear modulus N: number of Kuhn segments
		Eight-chain	1993	-	$[\mu, N]$	μ: is the shear modulus N: number of Kuhn segments
		Extended tube	1999	$0 < \beta \leq 1$	$[\mu_c, \mu_e, \beta, \delta]$	-

3 | EXPERIMENTAL

3.1 | Material

In this study, the hyperelastic behavior of a series of composite samples obtained from Borealis AB (Sweden) are made by mechanical mixing of CB filled EBA, with CB volume fraction ranging from 7.31% to 19.92%, is studied. The glass transition temperature of the dry EBA is $T_g \approx -75°C$ and the crystallinity determined by differential scanning calorimetry measurements is $X_C \approx 20$ vol%.[1] The average particle size of CB is 30 nm and the average size of the primary aggregates is typically 150 nm.[1] As illustrated by a SEM picture (Figure 1), the CB filler particles are finely dispersed in the EBA matrix.[29]

The chemical crosslinking of the elastomer is made by using peroxide agent. A second series of composite samples was immersed in a nonpolar solvent (toluene) at room-temperature for 72 h. The non-polarity of toluene permits to produce a high swelling ratio causing a drastic change in the microstructure of the swollen samples. The swelling process under free conditions was conducted as follows. At specific times, the samples are removed and, after blotting of the surfaces to remove excess liquid, the change of mass is recorded as a function of time by making use of a microbalance. This process is continued until the equilibrium state is attained corresponding to no change of weight. The samples swollen with this manner

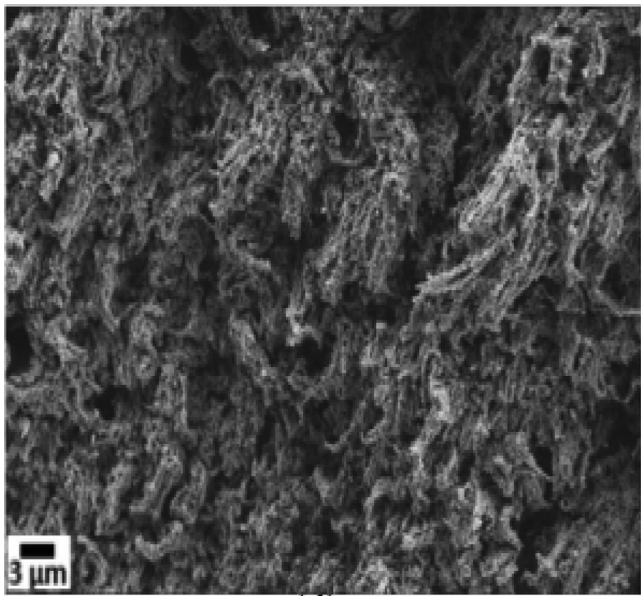

FIGURE 1 A typical SEM image of fractured surfaces of the CB/EBA sample containing 19.93% of CB particles. The scale bar corresponding to 3 µm.

are then axially stretched until moderated deformations typically (40%). As reported by us elsewhere,[29,30] a significant reduction of the mechanical properties was observed owing to the decrease of the effective crosslinks density υ_{cross}. For both dry and swollen samples, the υ_{cross} can be determined by

$$\upsilon_{cross} = \frac{1}{2 * M_c} \text{ with } G_P = \frac{\rho * R * T}{M_c}, \quad (20)$$

where, G_P is the strain hardening modulus, M_c is the molar mass between cross-links and ρ is the density.

In order to distinguish the chemical crosslink contribution generated by peroxide from the physical one by the CB particles, Flory-Rehner equation[31] is used

$$\upsilon_{cross} = -\frac{\ln(1-V_r) + V_r + X(0.434) * V_r^2}{2 * \rho_r * V_s * \left(\sqrt[3]{V_r} - \frac{V_r}{2}\right)}, \quad (21)$$

where, V_r denotes the volume fraction of the equilibrium swollen rubber with the filler, X is the polymer–solvent interaction parameter calculated according to Billmeyer's approach[7] and decreases with increasing the CB content, V_s denotes the molar volume of the solvent used (i.e., 106.27 cm^3/mol for toluene), and ρ_r is the neat elastomer density (see Table 2).

From Table 2, one can see that the physical crosslinks contribution to the total crosslinking degree is less than the chemical crosslinks, but it increases significantly as the CB volume fraction is increased. For the largest CB content investigated ($\emptyset = 19.93$ vol%), both contributions are similar.

The chemical crosslinks density can be calculated by substituting V_r to V_{r-f}, which represents the volume fraction of the equilibrium swollen neat elastomer. The V_{r-f} to V_r ratio varies linearly with $\left(\frac{\emptyset}{1-\emptyset}\right)$ according the Kraus equation.[32]

$$\frac{V_{r-f}}{V_r} = 1 - m\left(\frac{\emptyset}{1-\emptyset}\right), \quad (22)$$

where, $\emptyset$ denotes the CB volume fraction and m is the Kraus interaction between the elastomer and the filler particles. From Equation (19), m and V_{r-f} are found to be 0.68 and 0.51, respectively. Knowing the total crosslinks and the chemical crosslinks part, one can estimate the physical crosslinks part.

A schematic of the chemical and physical crosslinks in the microstructure of dry and swollen samples, showing the polymer and CB particle networks, is illustrated in Figure 2.

3.2 | Tensile tests

Room temperature tensile tests were performed using the mechanical testing machine model Instron 3369 on parallelepipedic samples with volume $70 \times 10 \times 2$ mm^3. All measurements were performed with a constant displacement speed of 2 mm min^{-1}. We confirm that no stress whitening, necking, or tearing of the samples was observed during tension tests. In particular, necking corresponds to the case for which the maximum stress keeps a constant value (or decreases) as the strain increases. This situation is not observed experimentally as can be observed from the stress–strain curves. Additionally, it is well now that the fractal CB network[1] allows deformation and damage (breakup of CB particles/aggregates and reorganization) in CB particles/elastomer composites to start from very low strain. Thence, no necking can occur.[33]

Uniaxial tensile stress consists in stretching along one direction one face of the specimen. With the following elongation $\lambda_1 = \lambda$, the other free facets of the sample do not experience any external stress and are in a zero stress state. The assumption of isotropy gives the other two principal extension ratios $\lambda_2 = \lambda_3 = \lambda^{-1/2}$.[34] We note that the extension λ is related to the strain ε according to the equation $\lambda = 1 + \varepsilon$.

The deformation gradient tensor F, Right Cauchy-Green tensor C, the left Gauchy-Green tensor B, and the three deformation invariants are

$$F = \begin{pmatrix} \lambda & 0 & 0 \\ 0 & 1/\sqrt{\lambda} & 0 \\ 0 & 0 & 1/\sqrt{\lambda} \end{pmatrix}, \quad (23)$$

TABLE 2 Chemical and physical crosslinks of EBA/CB composite samples swollen in toluene determined from swelling data coupled to the Flory and Kraus theories.

CB (vol%)	$\upsilon_{unswollen}$ (mol/g) $\times 10^{-4}$	$\upsilon_{swollen}$ (mol/g) $\times 10^{-4}$	ρ_r (g/cm^3)	V_r	X	S_i (%)	Chemical crosslinks (%)	Physical crosslinks (%)
7.31	30.30	9.66	0.933	0.531	1.137	75.28	89.86	10.14
10.84	40.66	13.2	0.951	0.579	1.007	68.81	65.76	34.24
13.10	48.46	12.89	0.969	0.576	0.853	57.84	67.34	32.66
15.92	58.90	13.53	0.985	0.584	0.822	55.09	64.15	35.85
19.93	72.40	16.49	1.013	0.616	0.745	46.81	52.64	47.36

Note: The values of the solvent–polymer interaction parameter X is calculated from Billmeyer's equation. The swelling index S_i is also included.

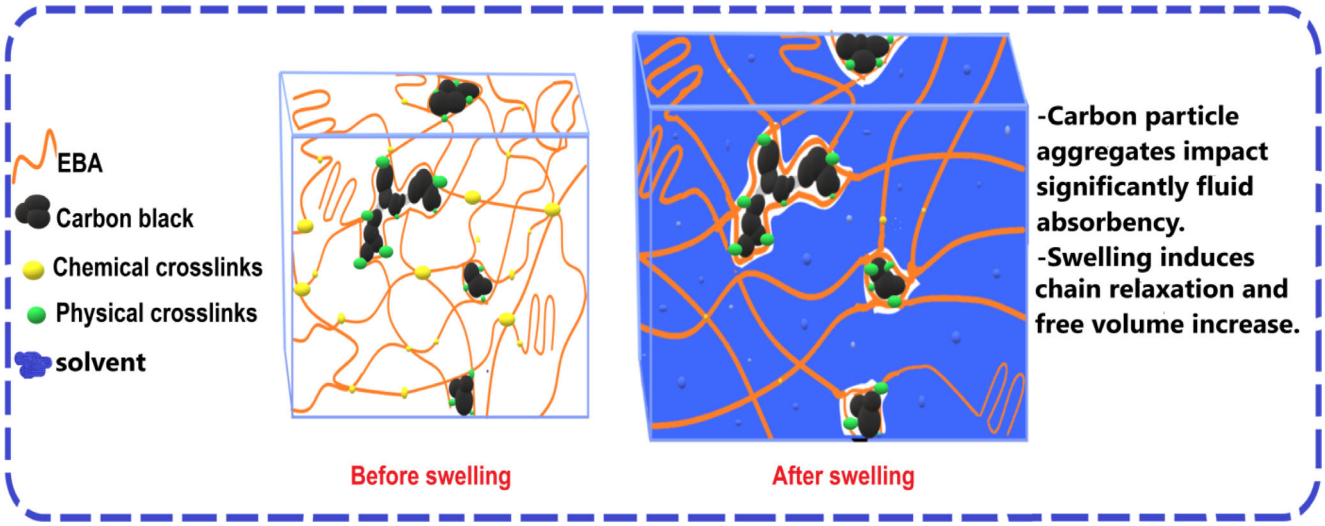

FIGURE 2 A schematic illustration of the effect of solvent (shown by the blue color) absorption on the microstructure of CB-EBA samples. [Color figure can be viewed at wileyonlinelibrary.com]

$$C = FF^T = \begin{pmatrix} \lambda & 0 & 0 \\ 0 & 1/\sqrt{\lambda} & 0 \\ 0 & 0 & 1/\sqrt{\lambda} \end{pmatrix} \begin{pmatrix} \lambda & 0 & 0 \\ 0 & 1/\sqrt{\lambda} & 0 \\ 0 & 0 & 1/\sqrt{\lambda} \end{pmatrix} = \begin{pmatrix} \lambda^2 & 0 & 0 \\ 0 & 1/\lambda & 0 \\ 0 & 0 & 1/\lambda \end{pmatrix}, \tag{24}$$

$$B = FF^T = \begin{pmatrix} \lambda & 0 & 0 \\ 0 & 1/\sqrt{\lambda} & 0 \\ 0 & 0 & 1/\sqrt{\lambda} \end{pmatrix} \begin{pmatrix} \lambda & 0 & 0 \\ 0 & 1/\sqrt{\lambda} & 0 \\ 0 & 0 & 1/\sqrt{\lambda} \end{pmatrix} = \begin{pmatrix} \lambda^2 & 0 & 0 \\ 0 & 1/\lambda & 0 \\ 0 & 0 & 1/\lambda \end{pmatrix}, \tag{25}$$

$$I_1 = tr(C) = \lambda^2 + \frac{2}{\lambda}, \tag{26}$$

$$I_2 = \frac{1}{2}\left[(tr(C))^2 - tr\left(C^2\right)\right] = 2\lambda + \frac{1}{\lambda^2}, \tag{27}$$

$$I_3 = det(C) = 1. \tag{28}$$

The Cauchy stress in the case of homogeneous uniaxial loading reads (see Appendix A)

$$\sigma_x = \left(\lambda^2 - \frac{1}{\lambda}\right)\left(\frac{\delta W}{\delta I_1} + \frac{1}{\lambda}\frac{\delta W}{\delta I_2}\right). \tag{29}$$

The uniaxial stress–strain analysis is implemented using OriginLab® Origin and programming with Matlab.

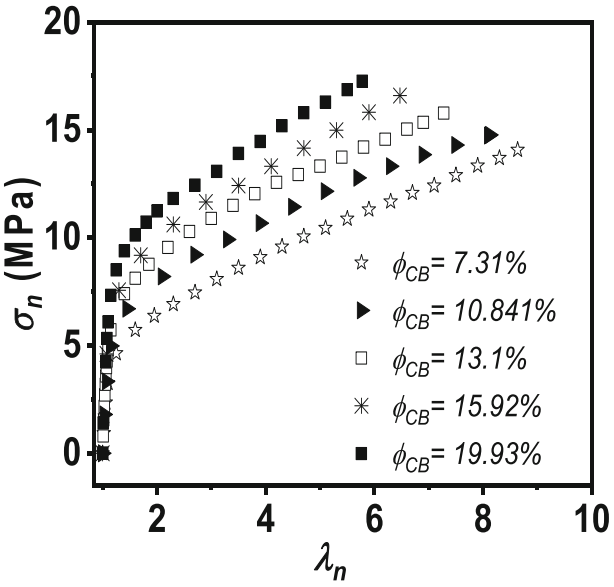

FIGURE 3 Effect of CB volume fraction on the stress–strain curves of CB-EBA samples during deformation.

4 | RESULTS AND DISCUSSION

As shown in Figure 3, the stress–strain responses of the CB-EBA samples exhibit a hyperelastic behavior. High deformations of the samples can be observed, for example, exceeding 800% for $\emptyset_{CB} = 7.31\%$.

It is important to note the significant and monotonically decrease of the polymer network elasticity is observed as the CB content increases. We attribute this λ dependent behavior to the fact that strain induced crystallization under uniaxial tension does not occur due to the increase of the crosslink density between the filler

particles surface and polymer chains.[17] The additional physical crosslinks hinder to some extent the relative displacement of the chain segments which are required for the nuclei formation and growth.[29,35,36]

4.1 | Modeling the hyperplastic behavior of CB filled EBA samples

To develop a quantitative understanding of this nonlinear elastic mechanical behavior we test the predictive ability of the models reviewed in Section 2 to correctly reproduce its dependence when a number of microstructure (CB content, effective crosslink density controlled by swelling in toluene as previously mentioned) and physical parameters (strain range) are varied.

4.1.1 | Analysis using phenomenological models

To model hyperelastic behavior, we use true stress $\sigma_v = \sigma_n(1+\varepsilon_n)$ and true strain $\varepsilon_v = (1+\varepsilon_n)$ to take account the substantial geometric changes during testing[37] where σ_n and ε_n are nominal stress and nominal strain respectively.

Modeling the stress–strain curve can be performed by either the 2-, 3-, 5-, or 9-parameter MR model.[38] Fitting the stress–strain curve with the 2-parameter MR model is not appropriate to represent the stress–strain data of CB filled EBA samples as reported elsewhere.[30] Because each curve is characterized by two inflection points, we find that the 5-parameter model (MR5) is more suitable to describe this nonlinear mechanical response of the stress–strain curves of our samples as illustrated in Figure 4a, in accordance with previous results of the archival literature.[38,39] The corresponding fitting parameters are listed in Table 3 and we observe that the correlation coefficient is found typically equal to 0.999.

It should be noted that the parameters of the MR5 model can distinguish the impact of chemical crosslinks (characterized by C_{10}) from that of the physical crosslinks (characterized by C_{01}).[40] Results show that the parameters C_{10} and C_{01} have similar increase as CB content is increased. Furthermore, since the value of C_{10} can be used to estimate the chemical crosslinking density according to $\upsilon_{cross} = |C_{10}|/RT$,[17,28,41,42] this indicates a linear increase of υ_{cross} as a function of CB content, in coherence with the reinforcing effect of the CB particles network. This is coherent since C_{10} is a measure of the deviation of linearity of the mechanical behavior with CB content.

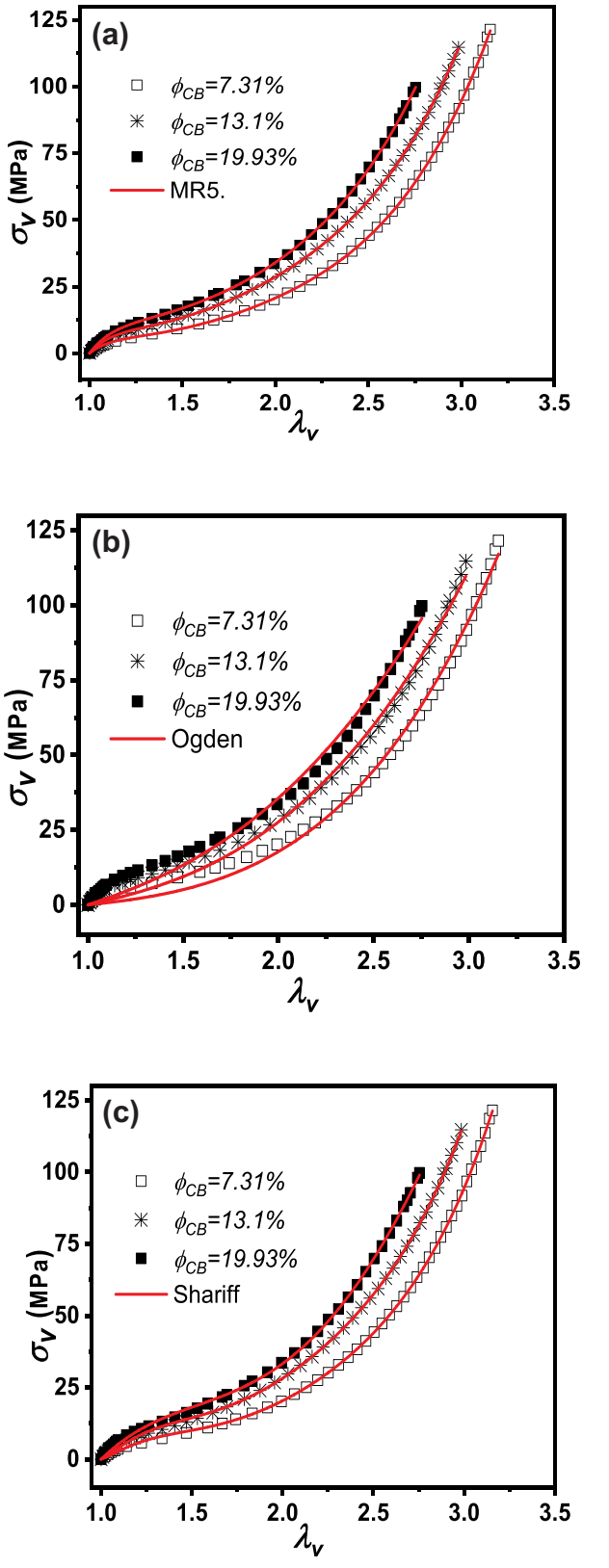

FIGURE 4 Modeling the experimental stress–strain curves. The symbols are data points and each red solid line represents a fitted behavior with a nonlinear function of the form: (a) MR model, (b) Ogden's model, and (c) Shariff's model. [Color figure can be viewed at wileyonlinelibrary.com]

TABLE 3 Relevant parameters of the curve fitting for the three phenomenological hyperelastic models.

	Parameters of the MR model (Equation 5)					
CB (vol%)	C_{10} (MPa)	C_{01} (MPa)	C_{11} (MPa)	C_{20} (MPa)	C_{02} (MPa)	R^2
19.93	−46.08	62.12	−10.97	2.72	26.96	0.999
15.92	−46.06	60.71	−14.92	2.53	32.48	0.999
13.10	−43.82	57.21	−11.87	2.76	27.99	0.999
10.84	−23.64	33.66	−4.40	1.25	12.20	0.999
7.31	−32.10	41.48	−9.89	21.71	3.73	0.999
	Parameters of the Ogden's model (Equation 7)					
	α_1	α_2	α_3	μ_1 (MPa)	μ_2 (MPa)	μ_3 (MPa)	R^2
19.93	2.97	0.00	0.00	4.75	0.00	0.00	0.990
15.92	3.25	0.00	0.00	3.34	0.00	0.00	0.991
13.10	3.38	0.00	0.00	2.75	0.00	0.00	0.994
10.84	3.66	0.00	0.00	1.86	0.00	0.00	0.995
7.31	4.11	0.00	0.00	1.04	0.00	0.00	0.996
	Parameters of the Shariff's model (Equation 10)				
	α_1	α_2	α_3	α_4	R^2
19.93	0.45	−1.32	−2.37	0.99	0.999
15.92	6.06	2.44	−20.46	−0.01	0.999
13.10	12.28	2.91	−35.21	0.22	0.999
10.84	2.66	0.70	−10.09	0.04	0.999
7.31	13.31	3.64	−39.22	0.13	0.999

Next, we investigate if Ogden's and Shariff's models can provide an accurate quantitative analysis of the stress–strain curves. To fit these curves with Ogden's model, a 3-term expansion of the SED function, that is, $k = 3$, is sufficient to describe the elastic mechanical response of rubber based-materials as reported by several studies.[9,28] As shown in Figure 4b this model provides a good description of the λ-dependent stress response of CB-EBA samples. The fitting parameters and correlation coefficients are listed in Table 3. As the CB volume fraction is increased we find that the model's prediction becomes less accurate at low deformations. This is because a large CB content strongly affects the mechanical response compared to the case of an ideal rubber.[11] Three remarks about the fitting parameters are in order. First, the values of the constants (α_r, μ_r) obtained for each CB content meet the stability condition $\alpha_r \mu_r > 0$.[28] Second, some parameters are found to be close to zero similarly to values found in Reference 14: this is because the complexity of the model is reduced by deactivating some terms of Ogden's model.[9] Third, the fitting parameter μ increases as CB content is increased. We also compare the experimental data to the quantitative estimate by using Shariff's model in Figure 4c. The obtained accuracy is similar to that reached by MR5. However, the obtained fitting parameters $\alpha_{i=1,4}$ (Table 3) do not follow the stability condition imposed by the model (Table 1).[25] Thence, our results suggest that Ogden's model is very robust to describe the hyper-elastic behavior of CB-EBA samples.

4.1.2 | Analysis with micro-mechanical models

Next, we examine the predictive ability of three micromechanical models to reproduce the hyperelastic behavior of CB-EBA samples under uniaxial tension. As shown in Figure 5a the experimental data are well represented by the analytical dependence of the extended tube model for three representative CB volume fractions.

The accuracy of this model for describing the experimental data is similar to that obtained by using Ogden's model. However, the fitting parameters (Table 4) are found to be discordant with the model assumptions (Table 1). Indeed, β should be in the range $(0 < \beta \leq 1)$[14] and this is not the case for CB-EBA samples.[28] Additionally, it remains hard to find a physical significance for the other fitting parameters which do not follow any simple

trend versus CB amount. For instance, μ_c which is related to the crosslinking part of the SED function should increase as CB content is increased. As illustrated in Figure 5b, the 3-chain model fails to accurately predict the mechanical response of CB-EBA samples. This is because the model is dominated by the contribution of the chains located along the maximum principal stretching directions and also due to its inherent affinity assumption.[9] Indeed, we expect that in a real network the chains along the maximum principal stretching direction would stretch less with further deformation once the extension limit is approached. At this point, other chains in the network stretch more than expected by the affine deformation in order to accommodate the total applied stretch. Thence, the affinity of the chain deformation is lost.[27] Contrary to the 3-chain model, the 8-chain model does not assume affine deformation for all chains.[14,28] This allows the 8-chain model to predict accurately the mechanical behavior of the CB-EBA samples as shown in Figure 5c. The values of the relevant fitting parameters μ and N are found to be similar (Table 4) to the typical values of elastomers.[9] In particular, μ shows a monotonically increase as CB volume fraction is increased as is expected from the reinforcing effect of the filler particles.

Overall, our results suggest that only MR and 8-chain models are able to accurately provide a quantitative estimate of the nonlinear elastic mechanical data of our CB-EBA samples. While both models have the merit to provide a physical understanding of their fitting parameters, the 8-chain model is preferable since it uses only two material constants. As can be expected, Ogden's model with five fitting parameters can be ranked in third position. On the other hand, the three other tested models (Shariff, extended tube, and 3-chain models) fail to accurately represent experimental data.

4.2 | Modeling the hyperplastic behavior of swollen CB-EBA samples

Next, we examine to what extent the MR, Ogden's and 8-chain's models can accurately describe the hyperelasticity of swollen CB-EBA samples in toluene. This solvent can produce a high swelling ratio ranging from 46% (high CB content) to 75% (low CB content) leading to significant change in the microstructure and elasticity network of swollen samples because the effective crosslinking density significantly decreases making the chains network more flexible. Furthermore, upon examination of the swelling behavior with the help of two suitable coupling diffusion-relaxation models, an earlier study[29] concluded that the relaxation mechanism dominates the swelling process compared to the diffusion mechanism. From the discussion in Reference 29, it can be also

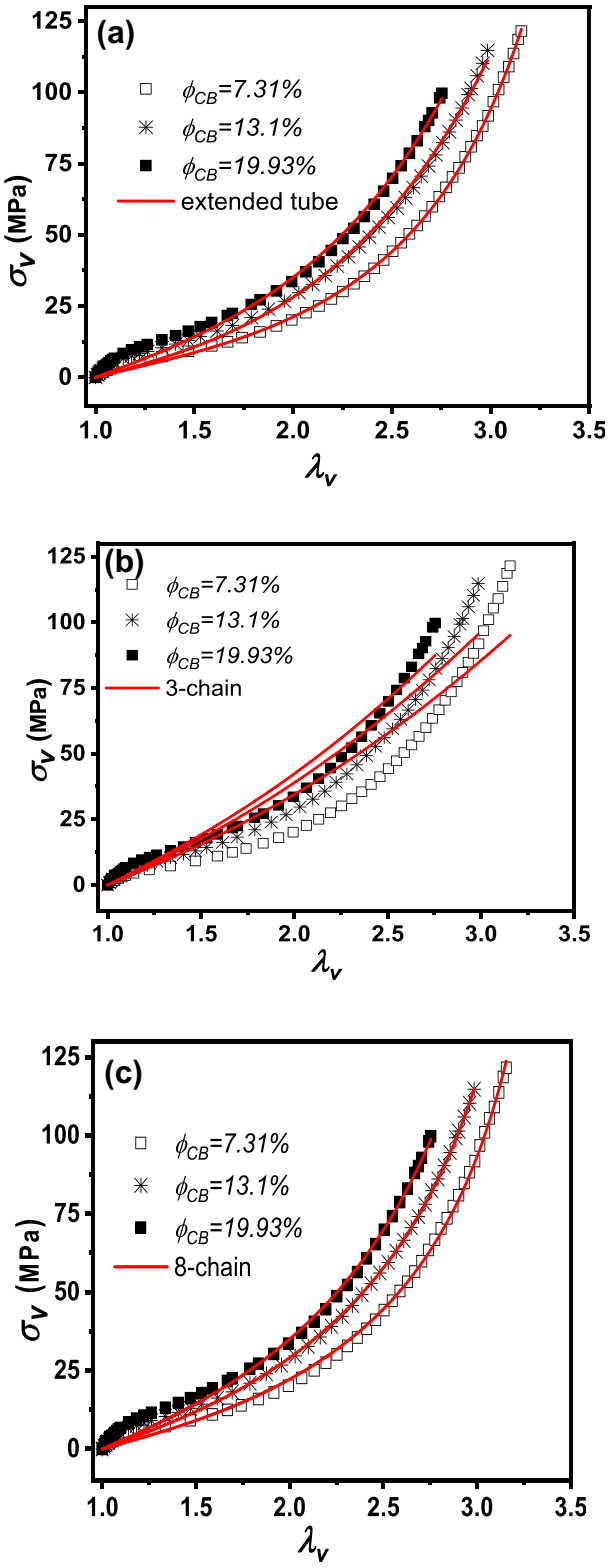

FIGURE 5 Modeling the experimental stress–strain curves. The symbols are data points and each red solid line represents a fitted behavior with a nonlinear function of the form: (a) extended tube model, (b) 3-chain model, and (c) 8-chain model. [Color figure can be viewed at wileyonlinelibrary.com]

concluded that swelling leads to an increase of the swollen sample volume, thus yielding to an increase of the

entanglement number. The significant changes in the microstructure (crosslinks, entanglements) of swollen samples directly affect their mechanical properties (Young modulus [E], strain hardening [G_p], and internal frictional forces [Y_0]) and eventually will modify the stress–strain response. Table 5 summarizes the change in several quantities between dry and swollen samples.[29]

4.2.1 | Analysis using MR, Ogden's and 8-chain models

The stress–strain behavior of our swollen samples is limited to 40% (see Figure 6) in order to avoid possible solvent evaporation when the sample is subjected to a large deformation over a long period of measurement time.

On the basis on the room temperature sorption/desorption experiments carried out in CB-EBA composites, it is found that the rate of desorption is faster than that of sorption, with a larger difference between both rates as CB content increases. This trend is consistent with experimental observations on similar composites.[43–45] Moreover, this trend is expected to be more pronounced when the swollen samples are subjected to uniaxial deformation due the volume expansion that can be caused by the separation between the polymer and the filler creating vacuoles.[46] For these reasons, in our experiment the maximal deformation is limited to 40%. The detail of the sorption/desorption results of CB-EBA samples is shown in Appendix B.

A quantitative estimate of the stress as a function of λ is shown in Figure 7. The material parameters corresponding to the three models are listed in Table 6.

Several remarks are in order. First, it is observed that the model's accuracy is very similar to that corresponding to the dry sample counterpart without any enhancement

TABLE 4 Material parameters and R^2 of curve fitting of micromechanical models.

	Parameters of the extended tube model (Equation 16)				
CB (vol%)	μ_c **(MPa)**	μ_e (MPa)	β	δ	R^2
19.93	0.33	8.28	−5.72	-8.51×10^{-8}	0.993
15.92	−2116.20	2132.90	−2.02	0.03	0.999
13.10	0.85	5.27	−4.78	-1.15×10^{-6}	0.996
10.84%	−1038.47	1050.67	−2.02	0.03	0.999
7.31%	1.76	4.57	3.03	0.23	0.999
	Parameters of the 8-chain model (Equation 14)				
	μ (MPa)		N	R^2	
19.93%	7.52		5.02	0.994	
15.92%	6.58		4.83	0.997	
13.1%	6.25		5.05	0.997	
10.84%	5.55		4.77	0.998	
7.31%	4.72		4.90	0.998	

TABLE 5 A comparison of the mechanical properties between dry and swollen CB-EBA samples.[29]

Material designation	CB (vol%)	E (MPa)	υ_{total} (mol/g) $\times 10^{-4}$	Y_0 (MPa)	G_p (MPa)	M_c (g/mol)
Dry samples	7.31	46.12	30.30	3.0	3.4	165.02
	10.84	63.76	40.66	3.9	4.2	122.85
	13.10	77.39	48.46	4.4	4.7	103.09
	15.92	96.32	58.90	4.7	5.25	84.89
	19.93	122.3	72.4	5.79	5.83	69.06
Swollen samples	7.31	13.88	9.66	0.5	2.5	517.38
	10.84	19.30	13.20	0.7	3.7	378.91
	13.10	19.18	12.89	0.8	4.1	387.89
	15.92	20.5	13.53	1	3.9	369.47
	19.93	25.70	16.49	1.3	4.2	303.18

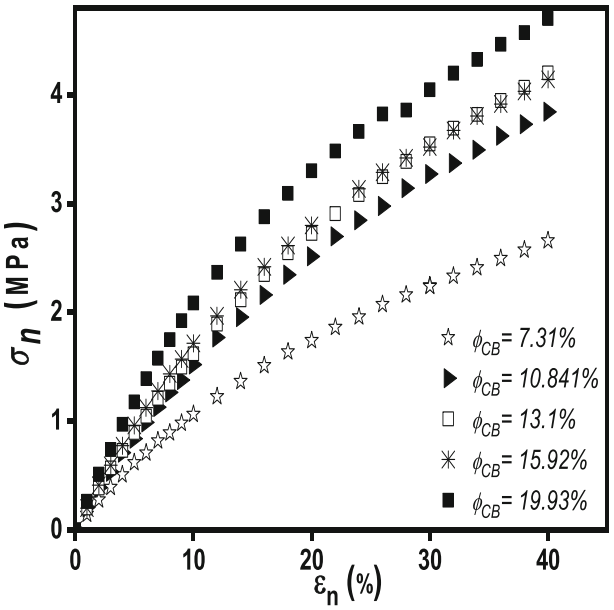

FIGURE 6 Stress–strain curves of swollen EBA as a function of CB content.

of the sample's elasticity. This makes the above ranking of these models practically unchanged. Second, from the fitting of the data of swollen and dry samples, a significant decrease of the fitting parameters having physical meaning $(C_{10}, C_{10}, \mu_1, \mu \text{ and } N)$ is observed. Hence, C_{10} and C_{01} decrease for swollen samples due to the decrease of the crosslinking density which is synonymous with a greater flexibility of the chain network. Furthermore, the solvent extraction of plasticizers and degradation of the physicochemical structure of the polymer network can also contribute to the decrease of both C_{10} and C_{01} as reported by Nohilé and coworkers.[40] Since the preferential localization of the solvent molecules in the bulk samples lies in the amorphous phase of the polymer, the observed decrease of the crosslinking density originates from the deterioration of chemical crosslinks, rather than the physical ones. However, no general trend is observed for the C_{10} dependence versus CB content. A similar explanation can be provided for the values of fitting parameters μ_1 and μ. Third, the complexity of the hyperelastic behavior of elastomers superimposes with the tortuosity of the 3D CB particle network which impacts toluene transport, and consequently affects the mechanical response of the swollen samples.

Considering the average R^2 value, the predictive performances of the MR, Ogden's and 8-chain models are summarized in Figure 8 for both swollen and dry CB-EBA samples.

All models provide good predictions, but the MR5 provides the most accurate quantitative measure of the

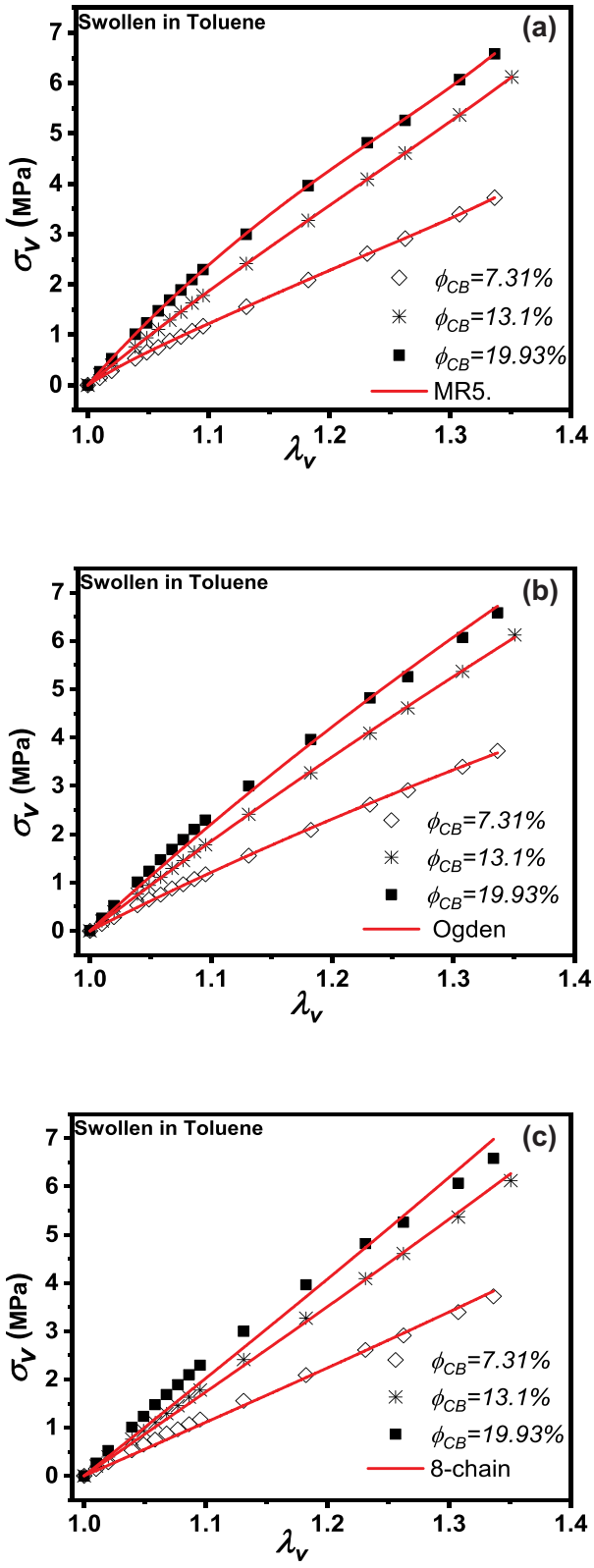

FIGURE 7 Modeling the experimental stress–strain curves. The symbols are data points and each red solid line represents a fitted behavior with a nonlinear function of the form: (a) MR, (b) Ogden's model, and (c) 8-chain model. [Color figure can be viewed at wileyonlinelibrary.com]

TABLE 6 Material parameters and correlation coefficients of the hyperelastic models applied to swollen CB-EBA samples.

	CB-EBA samples swollen with toluene					
	Parameters of the phenomenological MR model (Equation 5)					
CB (vol%)	C_{10} (MPa)	C_{01} (MPa)	C_{11} (MPa)	C_{20} (MPa)	C_{02} (MPa)	R^2
19.93	−3.07	7.63	−96.66	40.38	59.26	0.999
15.92	1.37	2.16	−2.02	2.92	−2.72	0.999
13.10	0.56	2.77	−7.76	3.58	4.65	0.999
10.84	−4.98	8.33	−119.02	45.55	81.73	0.999
7.31	−7.58	10.14	−135.75	51.38	94.88	0.999
	Parameters of the phenomenological Ogden's model (Equation 7)					
	α_1	α_2	α_3	μ_1 (MPa)	μ_2 (MPa)	μ_3 (MPa)	R^2
19.93	0.01	0.00	0.00	5465.13	0.00	0.00	0.995
15.92	0.01	0.00	0.00	3189.13	0.00	0.00	0.999
13.10	0.67	0.00	0.00	19.01	0.00	0.00	0.999
10.84	0.26	0.00	0.00	45.03	0.00	0.00	0.999
7.31	0.01	0.00	0.00	1283.49	0.00	0.00	0.999
	Parameters of the micro-mechanical 8-chain model (Equation 14)					
	μ (MPa)	N	R^2			
19.93	6.73	6.08×10^{17}	0.982			
15.92	5.89	5.25×10^{11}	0.995			
13.10	5.78	1.66×10^{15}	0.997			
10.84	4.02	3.38×10^{25}	0.993			
7.31	3.69	1.36×10^{43}	0.994			

stress–strain response of both dry and swollen CB-EBA samples over the range of CB volume fraction explored.

4.2.2 | Overall behavior of CB-filled elastomers

These findings underscore the structural parameters as an effective tool to tailor the effective mechanical properties of these nanostructured materials. If large deformation is desired, hysteresis loops appear after a load/unload cycle. This is the Mullins effect,[6] commonly attributed to an increase of the volume fraction of the soft part in the material, or to irreversible damage, or the combination of both effects. To observe this effect, CB-EBA samples are stretched at a fixed deformation followed by an unloading step. When a second loading is applied, the stress–strain curve is dropped below the curve obtained during the pre-stretching for a fixed deformation level and joints the first curve when the actual deformation exceeds the initial maximal deformation. A typical behavior is illustrated in Figure 9 for the sample containing 7.31 vol% of CB.

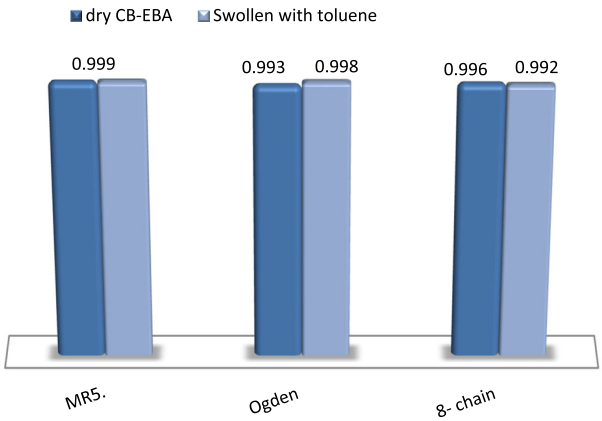

FIGURE 8 Correlation coefficient comparison of models to predict the hyperelastic behavior of CB-EBA under uniaxial tension for dry and swollen samples. [Color figure can be viewed at wileyonlinelibrary.com]

As can be seen from Figure 9, the softening characterized by a smaller stress at a given deformation, shows a gradual increase as the maximum deformation increases which was also found in Reference 47. Another interesting observation is the presence of a residual deformation

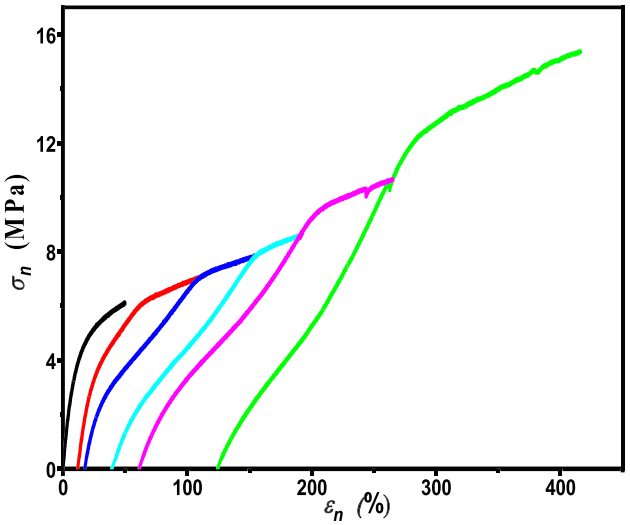

FIGURE 9 Stress–strain curves illustrating the Mullins effect for the CB-EBA sample, containing 7.31% of CB particles, subjected to different values of strain until fracture. [Color figure can be viewed at wileyonlinelibrary.com]

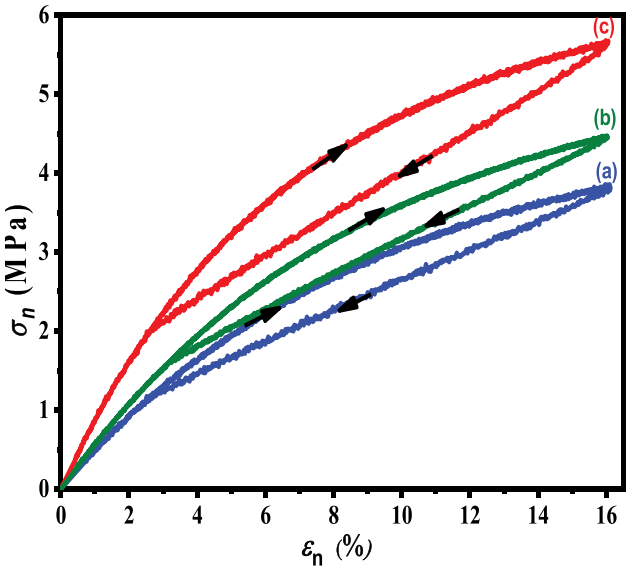

FIGURE 10 Stress–strain curves illustrating mechanical hysteresis after loading and unloading up to 16% deformation of CB-EBA samples with CB volume fractions: (a) 7.31, (b) 10.84, and (c) 13.10 vol%. [Color figure can be viewed at wileyonlinelibrary.com]

commonly called permanent set defined as the remaining extension after the sample is stretched and released. Like softening, this observed residual deformation increases with the amplitude of the applied strain. This observation is consistent with results reported by Dorfmann and Ogden on the CB filled natural rubber composites.[48] Consequently, the material highlighting a high softening shows also a high residual deformation as first noticed by Mullins.[49] We should emphasize that the softening phenomenon which is multidirectional induces anisotropy as earlier suggested by Mullins and experimentally observed in Reference 47 for many filled elastomer composites.

Different ways, for example, high temperature treatment, for complete recovery of the Mullins effect thanks to the reversibility of this physical phenomenon have been proposed in the literature. This aspect motivated a comprehensive review by Diani and coworkers.[47] From this study, it can be concluded that the use of most of the phenomenological mechanical models is limited to cases for which the induced anisotropy and residual deformation can be neglected. However, the details of the calculation of the characteristic length scale on which these phenomena should proceed remain unclear.

In another experiment, the stress–strain curves of loading/unloading cycles, for three samples containing 7.31, 10.84, and 13.10 vol% of CB particles, indicate that the hysteretic behavior is more and more visible as the CB content is increased (Figure 10). This result questions the above modeling presumption that there is no internal energy dissipation and partially explains the limitation of hyperelastic models. This result is supported by a recent study reported by He and coworkers,[8] where the authors concluded that the models performing excellent fitting results for the Treloar's data could not display superior performance for the test data of the highly filled hydrogenated nitrile-butadiene rubber.[8,50]

5 | CONCLUSION AND FINAL REMARKS

The experimental mechanical behavior of EBA filled with different CB content is compared to several predictive hyperelastic models by considering a single mode of deformation (uniaxial stretching). The ability of these models to reproduce the hyperelastic behavior is examined with regard to the change in microstructure generated either by the addition of CB particles or under swelling in toluene. Our results suggest that the increase in crosslink density due to the increase in CB content allows the polymer network to be less elastic. This increases the nonlinearity of the effective mechanical response of CB-EBA samples. Swelling decreases the crosslinking density and thus allows the polymer network to be more elastic. The robustness of each hyperelastic models is evaluated as function of the measured change in the elasticity of the material sample. Our results indicate that among six models investigated, three of them (MR, Ogden's, and 8-chain's model) are able to reproduce accurately the experimental behavior whatever the state of elasticity network of the stretched sample with an average coefficient of correlation of 0.999, 0.995,

and 0.994, respectively. The takeaway is that the fitting parameters of the MR model are well correlated to the structural changes in the sample, that is, crosslinking density. Similar correlation is also found in the case of the 8-chain model. Observe also that the accuracy of the Ogden's model slightly decreases as the CB volume fraction in the matrix is increased. Consistent with other work, for example, Reference 8 this study indicates that the superiority of the micromechanical models compared to the phenomenological ones is not a rule of thumb.

AUTHOR CONTRIBUTIONS

H. Boulman: Investigation (equal); methodology (equal); validation (equal); writing – original draft (equal). **A. Mdarhri:** Conceptualization (equal); formal analysis (equal); methodology (lead); supervision (lead); validation (equal); writing – original draft (lead); writing – review and editing (lead). **Y. Nezili:** Formal analysis (equal); investigation (equal); validation (equal); writing – original draft (equal). **F. El Haouzi:** Formal analysis (equal); investigation (equal); methodology (lead); validation (equal); writing – original draft (equal). **I. El Aboudi:** Investigation (equal); methodology (equal); supervision (equal); validation (equal); writing – original draft (equal); writing – review and editing (lead). **C. Brosseau:** Conceptualization (lead); formal analysis (equal); investigation (equal); supervision (equal); validation (equal); writing – original draft (lead); writing – review and editing (lead).

CONFLICT OF INTEREST STATEMENT

The authors declare that they have no known competing financial interests or personal relationships that could have appeared to influence the work reported in this article.

DATA AVAILABILITY STATEMENT

The data that support the findings of this study are available from the corresponding author upon reasonable request.

ORCID

A. Mdarhri https://orcid.org/0000-0001-7883-5700
C. Brosseau https://orcid.org/0000-0002-2629-0267

REFERENCES

[1] F. Elhaouzi, A. Nourdine, C. Brosseau, A. Mdarhri, I. El Aboudi, M. Zaghrioui, *Polym. Compos.* **2019**, *40*, 8.
[2] T. Gehling, J. Schieppati, W. Balasooriya, R. C. Kerschbaumer, G. Pinter, *Polym. Rev.* **2023**, *63*, 763.
[3] G. M. Bristow, *J. Polymer Sci. A* **1963**, *1*, 2261.
[4] P. M. Visakh, S. Thomas, A. K. Chandra, A. P. Mathew, *Advances in Elastomers II: Composites and Nanocomposites (Advanced Structured Materials Book 12)*, Springer, Berlin, Germany **2013**.
[5] J. Kallungal, L. Chazeau, J. M. Chenal, J. Adrien, E. Maire, C. Barrès, B. Cantaloube, P. Heuillet, F. Wilde, J. Moosmann, T. Weitkamp, *Eng. Fract. Mech.* **2023**, *277*, 109007.
[6] L. Chazeau, C. Gauthier, G. Vigier, J. Y. Cavaillé, *Handbook of Organic-Inorganic Hybrid Materials and Nanocomposites* (Ed: H. S. Nalwa), Vol. 2, American Scientific Publishers, Valencia, California **2003**.
[7] F. W. Billmeyer, *Textbook of Polymer Science*, Wiley, New York **1984**.
[8] H. He, Q. Zhang, Y. Zhang, J. Chen, L. Zhang, F. Li, *NMS* **2022**, *4*, 2.
[9] S. K. Melly, L. Liu, Y. Liu, J. Leng, *IJMSD* **2021**, *1*, 1.
[10] A. Ricker, P. Wriggers, *Arch. Comput. Methods Eng.* **2023**, *30*, 3.
[11] H. Dal, Y. Badienia, K. Acikgoz, F. A. Denli, *Const. Models Rubber* **2019**, *XI*, 239.
[12] P. Mazur, R. W. Ogden, *Non-Linear Elastic Deformations*, Courier Corporation, Massachusetts United States **1997**.
[13] G. Marckmann, E. Verron, *Rubber Chem. Technol.* **2006**, *79*, 5.
[14] P. Steinmann, M. Hossain, G. Possart, *Arch. Appl. Mech.* **2012**, *82*, 1183.
[15] O. H. Yeoh, *Rubber Chem. Technol.* **1990**, *63*, 5.
[16] P. Haupt, K. Sedlan, *Arch. Appl. Mech.* **2001**, *71*, 89.
[17] M. Fujikawa, N. Maeda, J. Yamabe, M. Koishi, *Rubber Chem. Technol.* **2020**, *93*, 1.
[18] X. Li, Z. Li, Y. Xia, *Rubber Chem. Technol.* **2015**, *88*, 1.
[19] Y. Yamashita, S. Kawabata, *JSRIJ* **1992**, *65*, 9.
[20] A. Lion, *Contin. Mech. Thermodyn.* **1996**, *8*, 153.
[21] F. Laraba-abbes, P. Ienny, R. Piques, *Polymer* **2003**, *44*, 3.
[22] D. J. Seibert, N. Schoche, *Rubber Chem. Technol.* **2000**, *73*, 2.
[23] J. S. Bergstrom, *Mechanics of Solid Polymers: Theory and Computational Modeling Elsevier*, Amsterdam, Netherlands **2015**.
[24] M. Mooney, *J. Appl. Phys.* **1940**, *11*, 9.
[25] M. H. B. M. Shariff, *Rubber Chem. Technol.* **2000**, *73*, 1.
[26] Y. Dong, R. J. T. Lin, D. Bhattacharyya, *J. Mater. Sci.* **2005**, *40*, 399.
[27] M. C. Boyce, E. M. Arruda, *Rubber Chem. Technol.* **2000**, *73*, 3.
[28] M. Hossain, P. Steinmann, *J. Mech. Behav. Mater.* **2013**, *22*, 1.
[29] Y. Nezili, A. Mdarhri, I. El Aboudi, C. Brosseau, M. Zaghrioui, A. Ghorbal, D. He, J. Bai, *Polymer* **2023**, *264*, 125563.
[30] F. Elhaouzi, A. Mdarhri, C. Brosseau, I. El Aboudi, A. Almaggoussi, *Polym. Bull.* **2019**, *76*, 2765.
[31] P. J. Flory, J. Rehner, *J. Chem. Phys.* **1943**, *11*, 11.
[32] G. Kraus, *J. Appl. Polym. Sci.* **1963**, *7*, 3.
[33] P. Millereau, E. Ducrot, J. M. Clough, M. E. Wiseman, H. R. Brown, R. P. Sijbesma, C. Creton, *PNAS* **2018**, *115*, 37.
[34] J. Dispersyn, S. Hertelé, W. De Waele, J. Belis, *Int. J. Adhes. Adhes.* **2017**, *77*, 102.
[35] L. R. Treloar, *OUP* **1975**, *351*, 1666.
[36] Z. Bouyahia, A. Mdarhri, A. Benayad, C. Brosseau, I. El Aboudi, D. Chicot, A. Iost, D. He, J. Bai, *J. Appl. Polym. Sci.* **2021**, *138*, 29.
[37] H. Boulman, A. Mdarhri, I. El Aboudi, C. Brosseau, O. Lame, D. He, J. Bai, *Polymer* **2022**, *258*, 125325.
[38] N. Kumar, V. V. Rao, *Int. J. Mech. Eng.* **2016**, *6*, 1.
[39] S. Zulfiqar, A. A. Saad, Z. Ahmad, F. Yusof, K. Fakpan, *J. Adv. Manuf. Technol.* **2022**, *16*, 1.
[40] C. Nohilé, Doctoral Thesis, Diss. SAT. **2010**.
[41] S. Arévalo-Alquichire, C. Dominguez-paz, M. F. Valero, *Materials* **2020**, *13*, 21.
[42] S. Vishvanathperumal, V. Navaneethakrishnan, G. Anand, S. Gopalakannan, *ASEM* **2020**, *12*, 5.

[43] K. Priya Dasan, G. Unnikrishnan, E. Purushothaman, *Polym. Polym. Compos.* **2008**, *2*, 2.
[44] K. Dasan, A. P. Haseena, G. Unnikrishnan, R. Alex, E. Purushothama, *Polym. Polym. Compos.* **2004**, *2*, 7.
[45] S. V. Nair, M. S. Sreekala, G. Unnikrishnan, T. Johnson, S. Thomas, G. Groeninckx, *J. Membr. Sci.* **2000**, *177*, 1.
[46] G. Kraus, C. W. Childers, K. W. Rollmann, *J. Appl. Polym. Sci.* **1966**, *10*, 2.
[47] J. Diani, B. Fayolle, P. Gilormini, *Eur. Polym. J.* **2009**, *45*, 3.
[48] A. Dorfmann, R. W. Ogden, *Int. J. Solids Struc.t* **2004**, *41*, 7.
[49] L. Mullins, *Rubber Chem. Technol.* **1949**, *22*, 4.
[50] T. W. Ohenberger, R. J. Windslow, N. M. Pugno, J. J. Usfield, *Rubber Chem. Technol.* **2019**, *92*, 4.

How to cite this article: H. Boulman, A. Mdarhri, Y. Nezili, F. El Haouzi, I. El Aboudi, C. Brosseau, *J. Appl. Polym. Sci.* **2024**, *141*(13), e55168. https://doi.org/10.1002/app.55168

APPENDIX A: DETERMINATION OF THE PRINCIPAL CAUCHY STRESS IN UNIAXIAL TENSION FOR AN INCOMPRESSIBLE MATERIAL

This appendix is dedicated to the determination of the Cauchy stress for incompressible uniaxial loading.[13,23,24] To satisfy the Clausius-Duhem inequality, the Cauchy stress for a thermoelastic material reads

$$\sigma(\boldsymbol{F},\theta_0)=\frac{1}{J}\frac{\delta W(\boldsymbol{F},\theta_0)}{\delta \boldsymbol{F}}\boldsymbol{F}^T, \tag{A1}$$

where, w is the Helmholtz free energy per unit current volume, $\boldsymbol{F}$ is the deformation gradient, J is the Jacobian determinant and θ_0 denotes the temperature. A change of observer implies that the stress and the Helmholtz free energy have the following functional forms

$$\sigma(\boldsymbol{F})=\boldsymbol{R}\,\sigma(\boldsymbol{U})\boldsymbol{R}^T=\boldsymbol{R}\,\sigma(\boldsymbol{C})\boldsymbol{R}^T\sigma(\boldsymbol{F})=\boldsymbol{R}\,\sigma(\boldsymbol{U})\boldsymbol{R}^T=\boldsymbol{R}\,\sigma(\boldsymbol{C})\boldsymbol{R}^T, \tag{A2}$$

where, $\boldsymbol{U}$ is the right stretch tensor, $\boldsymbol{C}$ denotes the right Cauchy-Green tensor, and $\boldsymbol{R}$ is the rotation tensor. Now writing

$$W(\boldsymbol{F},\theta_0)=W(\boldsymbol{U},\theta_0)=W(\boldsymbol{C},\theta_0), \tag{A3}$$

and inserting it into (A1) leads to

$$\sigma(\boldsymbol{U},\theta_0)=\boldsymbol{R}\left[\frac{1}{J}\frac{\delta W(\boldsymbol{U},\theta_0)}{\delta \boldsymbol{U}}\boldsymbol{U}^T\right]\boldsymbol{R}^T. \tag{A4}$$

The partial derivative $\frac{\delta W(\boldsymbol{U},\theta_0)}{\delta \boldsymbol{U}}$ can be written as

$$\frac{\delta W(\boldsymbol{U},\theta_0)}{\delta \boldsymbol{U}}=2\boldsymbol{U}\frac{\delta W(\boldsymbol{C})}{\delta \boldsymbol{C}}. \tag{A5}$$

Then, Equation (A4) becomes

$$\sigma(\boldsymbol{C},\theta_0)=\frac{2}{J}\boldsymbol{F}\frac{\delta W(\boldsymbol{C},\theta_0)}{\delta \boldsymbol{C}}\boldsymbol{F}^T. \tag{A6}$$

Using the expressions of the strain invariants of the Cauchy-Green tensor I_1, I_2, and I_3

$$I_1=tr(\boldsymbol{C})=\lambda^2+\frac{2}{\lambda}, \tag{A7}$$

$$I_2=\frac{1}{2}\left[(tr(\boldsymbol{C}))^2-tr\left(\boldsymbol{C}^2\right)\right]=2\lambda+\frac{1}{\lambda^2}, \tag{A8}$$

$$I_3=det(\boldsymbol{C})=1, \tag{A9}$$

the Helmholtz free energy can be written as $w(I_1,I_2,I_3,\theta_0)$ and Equation (A6) reads

$$\sigma(\boldsymbol{C},\theta_0)=\frac{2}{J}\boldsymbol{F}\left[\frac{\delta W}{\delta I_1}\frac{\delta I_1}{\delta \boldsymbol{C}}+\frac{\delta W}{\delta I_2}\frac{\delta I_2}{\delta \boldsymbol{C}}+\frac{\delta W}{\delta I_3}\frac{\delta I_3}{\delta \boldsymbol{C}}\right]\boldsymbol{F}^T. \tag{A10}$$

From Equations (A11)–(A13), one obtains

$$\frac{\delta I_1}{\delta \boldsymbol{C}}=I, \tag{A11}$$

$$\frac{\delta I_2(\boldsymbol{C})}{\delta \boldsymbol{C}}=I_1 I-\boldsymbol{C}, \tag{A12}$$

$$\frac{\delta I_3(\boldsymbol{C})}{\delta \boldsymbol{C}}=I_3\boldsymbol{C}^{-1}=I_3\boldsymbol{F}^{-1}\boldsymbol{F}^{-T}. \tag{A13}$$

Now Equation (A10) becomes

$$\begin{aligned}&\sigma(I_1,I_2,I_3,\theta_0)\\&=\frac{2}{J}\boldsymbol{F}\left[\frac{\delta W}{\delta I_1}I+\frac{\delta W}{\delta I_2}(I_1 I-\boldsymbol{C})+\frac{\delta W}{\delta I_3}I_3\boldsymbol{C}^{-1}\right]\boldsymbol{F}^T\\&=\frac{2}{J}\left[\left(\frac{\delta W}{\delta I_1}+I_1\frac{\delta W}{\delta I_2}\right)\boldsymbol{b}-\frac{\delta W}{\delta I_2}\boldsymbol{b}^2+I_3\frac{\delta W}{\delta I_3}I\right]\\&=2\left[\left(\frac{\delta W}{\delta I_1}+I_1\frac{\delta W}{\delta I_2}\right)\boldsymbol{b}-\frac{\delta W}{\delta I_2}\boldsymbol{b}^2\right]-pI.\end{aligned} \tag{A14}$$

Note that the left Cauchy-Green tensor $\boldsymbol{b}$, and the right Cauchy-Green $\boldsymbol{C}$ tensor can be expressed as a function of the deformation gradient $\boldsymbol{F}$ as $\boldsymbol{b}=\boldsymbol{F}\boldsymbol{F}^T$ and $\boldsymbol{C}=\boldsymbol{F}^T\boldsymbol{F}$, respectively.

Therefore, for uniaxial traction, the deformation gradient is given by

$$\mathbf{F}=\begin{pmatrix}\lambda & 0 & 0\\ 0 & 1/\sqrt{\lambda} & 0\\ 0 & 0 & 1/\sqrt{\lambda}\end{pmatrix}. \tag{A15}$$

Then, the left Cauchy-Green tensor is given by

$$\boldsymbol{b}=\boldsymbol{F}\boldsymbol{F}^T=\begin{pmatrix}\lambda & 0 & 0\\ 0 & 1/\sqrt{\lambda} & 0\\ 0 & 0 & 1/\sqrt{\lambda}\end{pmatrix}\begin{pmatrix}\lambda & 0 & 0\\ 0 & 1/\sqrt{\lambda} & 0\\ 0 & 0 & 1/\sqrt{\lambda}\end{pmatrix}=\begin{pmatrix}\lambda^2 & 0 & 0\\ 0 & 1/\lambda & 0\\ 0 & 0 & 1/\lambda\end{pmatrix}, \tag{A16}$$

$$\boldsymbol{b}^2=\begin{pmatrix}\lambda^4 & 0 & 0\\ 0 & 1/\lambda^2 & 0\\ 0 & 0 & 1/\lambda^2\end{pmatrix}, \tag{A17}$$

and

$$\boldsymbol{C}=\boldsymbol{F}^T\boldsymbol{F}=\begin{pmatrix}\lambda^2 & 0 & 0\\ 0 & 1/\lambda & 0\\ 0 & 0 & 1/\lambda\end{pmatrix}, \tag{A18}$$

where

$$\begin{aligned}\sigma_x&=2\left[\left(\frac{\delta W}{\delta I_1}+\left(\lambda^2+\frac{2}{\lambda}\right)\frac{\delta W}{\delta I_2}\right)\lambda^2-\frac{\delta W}{\delta I_2}\lambda^4\right]-p\\&=2\left[\frac{\delta W}{\delta I_1}\lambda^2+2\lambda\frac{\delta W}{\delta I_2}\right]-p,\end{aligned} \tag{A19}$$

$$\sigma_y=\sigma_z=2\left[\left(\frac{\delta W}{\delta I_1}+\left(\lambda^2+\frac{2}{\lambda}\right)\frac{\delta W}{\delta I_2}\right)\frac{1}{\lambda}-\frac{\delta W}{\delta I_2}\frac{1}{\lambda^2}\right]-p=0, \tag{A20}$$

$$p=2\left[\left(\frac{\delta W}{\delta I_1}+\left(\lambda^2+\frac{2}{\lambda}\right)\frac{\delta W}{\delta I_2}\right)\frac{1}{\lambda}-\frac{\delta W}{\delta I_2}\frac{1}{\lambda^2}\right], \tag{A21}$$

$$\begin{aligned}\sigma_x&=2\left[\frac{\delta W}{\delta I_1}\lambda^2+2\lambda\frac{\delta W}{\delta I_2}\right]-2\left[\left(\frac{\delta W}{\delta I_1}+\left(\lambda^2+\frac{2}{\lambda}\right)\frac{\delta W}{\delta I_2}\right)\frac{1}{\lambda}-\frac{\delta W}{\delta I_2}\frac{1}{\lambda^2}\right]\\&=2\left[\frac{\delta W}{\delta I_1}\lambda^2-\frac{\delta W}{\delta I_2}\frac{1}{\lambda^2}+\lambda\frac{\delta W}{\delta I_2}-\frac{1}{\lambda}\frac{\delta W}{\delta I_1}\right].\end{aligned} \tag{A22}$$

Finally, the Cauchy stress is expressed by

$$\sigma_{uniax}=\left(\lambda^2-\frac{1}{\lambda}\right)\left(\frac{\delta W}{\delta I_1}+\frac{1}{\lambda}\frac{\delta W}{\delta I_2}\right). \tag{A23}$$

APPENDIX B: KINETICS OF SOLVENT SORPTION/DESORPTION IN EBA/CB COMPOSITE SAMPLES UNDER FREE-SWELLING CONDITIONS IN TOLUENE

To compare the sorption/desorption kinetics in the CB-EBA composites, both time variations of the percentage of toluene sorption $Q_{t,sorption}$ and desorption $Q_{t,desorption}$ are measured at room temperature according to the experimental protocol detailed elsewhere.[29,30] Then, $Q_{t,sorption}$ and $Q_{t,desorption}$ (mol%) are calculated from

$$Q_{t,sorption}(\text{mol}\%)=\frac{m_t-m_0}{m_0.M_s}\times 100, \tag{B1}$$

and

$$Q_{t,desorption}(\text{mol}\%)=\frac{m_{t-}m_{eq}}{m_{eq}.M_s}\times 100, \tag{B2}$$

respectively, where m_0 is the initial mass, m_t is the mass at time t, m_{eq} is the mass at equilibrium, and M_s denotes the molar mass of solvent. Figure B1 illustrates the kinetics of solvent sorption (black) and desorption (red) isotherms in EBA containing (a) 7.31, (b) 13.10, and (c) 19.93 vol% of CB, respectively.

From these results, the rate of desorption is found to be larger than the rate of sorption especially in the first stage of the kinetic curves. This behavior is consistent with the results reported in other studies.[43–45] In the first stage, the sorption/desorption data after 1 h which is

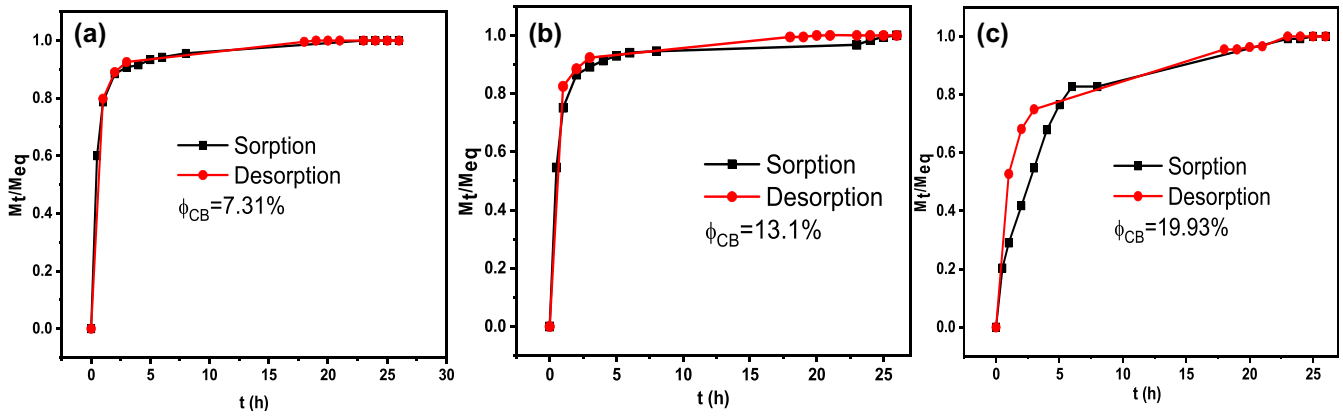

FIGURE B1 Kinetics of toluene sorption (black) and desorption (red) in CB-EBA samples containing different CB volume fractions. Room temperature. [Color figure can be viewed at wileyonlinelibrary.com]

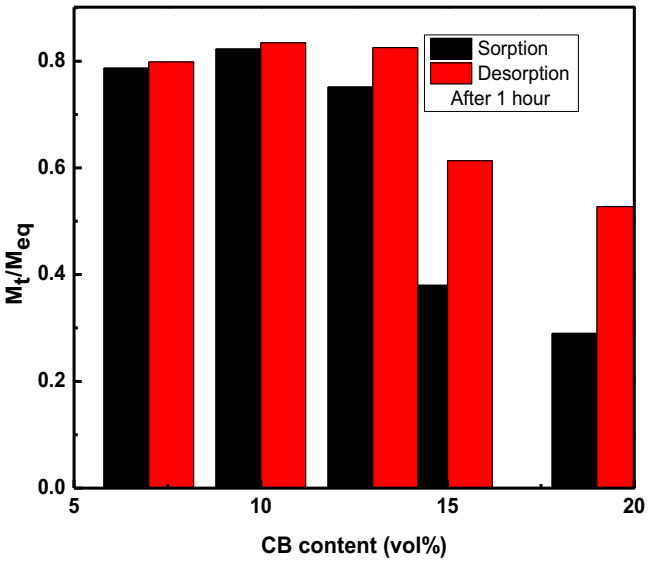

FIGURE B2 Comparison of the rate of sorption (black) and desorption (red) in toluene of CB-EBA samples with different CB volume fractions occurring in the first stage of sorption/desorption curves, that is, after 1 h. Room temperature. [Color figure can be viewed at wileyonlinelibrary.com]

sufficient time to perform tensile tests are shown in Figure B2 for all CB content investigated.

From this figure, the difference between the sorption and desorption rates increases as the CB amount increases because the CB aggregates act as obstacles against solvent molecules transport inside the elastomer matrix, thus facilitating the desorption process. Additionally, this trend is expected to be more pronounced when the swollen samples are subjected to uniaxial deformation due the volume expansion which is caused by the separation between the polymer chains and the filler particles creating vacuoles.[46] For these reasons, the maximal deformation is limited to 40%.